

DBMovi-GS: Dynamic View Synthesis from Blurry Monocular Video via Sparse-Controlled Gaussian Splatting

Yeon-Ji Song^{1,3}, Jaein Kim^{1,3}, Byung-Ju Kim^{2,3}, Byoung-Tak Zhang^{1,2,3*}

¹Interdisciplinary Program in Neuroscience ²IPAI ³AIS, Seoul National University

Abstract

Novel view synthesis is a task of generating scenes from unseen perspectives; however, synthesizing dynamic scenes from blurry monocular videos remains an unresolved challenge that has yet to be effectively addressed. Existing novel view synthesis methods are often constrained by their reliance on high-resolution images or strong assumptions about static geometry and rigid scene priors. Consequently, their approaches lack robustness in real-world environments with dynamic object and camera motion, leading to instability and degraded visual fidelity. To address this, we propose Motion-aware **D**ynamic **V**iew **S**ynthesis from **B**lurry **M**onocular **V**ideo via **S**parse-**C**ontrolled **G**aussian **S**platting (DBMovi-GS), a method designed for dynamic view synthesis from blurry monocular videos. Our model generates dense 3D Gaussians, restoring sharpness from blurry videos and reconstructing detailed 3D geometry of the scene affected by dynamic motion variations. Our model achieves robust performance in novel view synthesis under dynamic blurry scenes and sets a new benchmark in realistic novel view synthesis for blurry monocular video inputs.

1. Introduction

3D Gaussian Splatting (3DGS) [14] has emerged as a promising tool for photorealistic scene reconstruction and novel view synthesis, offering real-time rendering, improved efficiency, and reduced training time. However, 3DGS faces challenges in complex real-world settings, particularly in dynamic, multi-object, and blurry scenes [3, 31]. A critical prerequisite for effective 3DGS is the accurate point cloud initialization, usually handled by the Structure-from-Motion (SfM) [32] implementations such as COLMAP [30]. Inaccuracies in SfM initialization and difficulties in simultaneous camera and object motion estimation limit its applicability to static, high-resolution inputs. Consequently, existing 3DGS-based methods are challenged by long-exposure inputs, varying lighting condi-

Model	Image Deblurring			View Synthesis
	Defocus Blur	Camera Motion Blur	Object Motion Blur	Camera Pose Trajectory
Deblur-GS[5]	✓	✓	✗	✗
Deblurring 3DGS[16]	✓	✗	✓	✗
Nope NeRF[3]	✗	✓	✗	✓
GS on the Move[31]	✗	✓	✗	✓
Colmap-Free[9]	✗	✓	✗	✓
Ours	✓	✓	✓	✓

Table 1. Summary of capabilities addressed in the previous models. In our work, the abbreviation for image deblurring models and view synthesis models are “id” and “vs”, respectively.

tions, and camera-induced motion blur. Common sources of real-world blur further degrade reconstruction quality and introduce artifacts in synthesized views.

Recent research has aimed to reduce reliance on SfM techniques due to inaccurate and sparse Gaussian point initialization [8, 9]. These approaches integrate pose estimation within the view synthesis frameworks, addressing joint photorealistic scene reconstruction and camera pose estimation. However, current methods are limited to specific scenarios, such as linear, slow-moving camera trajectories around a single object [22, 35, 36], or address scenes with complex camera trajectories, yet typically rely on moderate to high-resolution inputs [7, 21, 27]. Table 1 summarizes the capabilities of existing methods. Most focus on implicit neural field representations rather than direct camera pose optimization, presenting challenges for substantial camera movements. Despite advancements, prolonged training times and diminished performance remain challenges in the joint novel view synthesis and camera pose estimation for multi-object blurry environments [3, 33].

With this motivation, we aim to enhance the robustness and versatility of novel view synthesis in dynamically complex real-world scenarios while handling a variety of blur effects. To this end, we propose DBMovi-GS, a novel dynamic view synthesis method for blurry monocular videos. DBMovi-GS is designed to handle three common types of blur encountered in real-world environments:

*Correspondence to btzhang@snu.ac.kr.

camera motion blur, object motion blur, and defocus blur. We conduct an in-depth analysis of Gaussian initialization to derive dense 3D Gaussians from sparse points. These Gaussians facilitate the robust modeling of object motion and camera pose, enabling photorealistic scene reconstruction in dynamic real-world scenarios. Experimental results demonstrate that our model achieves superior performance in novel view synthesis and deblurring, effectively adapting to real-world scenes. Additionally, our work integrates seamlessly with rasterization techniques, enabling real-time rendering while preserving high-fidelity view synthesis.

2. Related Work

2.1. Dynamic View Synthesis

Dynamic View Synthesis focuses on generating novel views of dynamic scenes, capturing both object motion and viewpoint changes across time. While multi-view [2, 19], stereo [1], and sparse-view [12] cameras have made progress, monocular videos remain challenging due to single-viewpoint ambiguities. Earlier works utilize geometric priors, such as depth [6, 28] and optical flow [20, 40], or deformable radiance fields and regularization [24, 25] to enhance reconstruction but often remain constrained to specific scenarios, limiting generalizability [21]. Inspired by 3DGS, recent works achieve improved rendering quality [7, 21] or represent dynamic scenes with optimized Gaussians [23, 38]. Another line of work focuses on camera pose estimation [9] or image deblurring [5, 16] separately, limiting their ability to achieve view synthesis with motion-related blur effects. Building on prior work, our approach models both object and camera motion to achieve realistic view synthesis in challenging blurry environments.

2.2. Deblurring 3D Representations

Image deblurring has become a critical task, especially with the growing demand for high-quality visuals in real-world applications. Recent methods leverage NeRF [4, 25, 26] and Gaussian splatting [5, 16] due to their effectiveness in scene reconstruction. NeRF-based approaches incorporate blur kernels with physical priors or model camera trajectories [33] and voxel-based camera motions [18], showing efficiency in highly blurred images, but often rely on pretrained models [17] or lack 3D scene consistency [25]. Gaussian splatting-based approaches address blurry 3D scenes and probabilistic point rendering through camera motion trajectory modeling [5, 9, 16]. While prior works excel in addressing defocus blur [16] or camera motion blur [5, 9], they often struggle with object motion blur and fine detail preservation. Our model effectively handles various blur types and improves the accuracy of object and pose estimation while preserving the fine scene details.

3. Method

DBMovi-GS aims to reconstruct dynamic scenes from blurry monocular videos. We detail our approach for sparse-controlled Gaussian Splatting, followed by techniques for modeling object and camera motion. Lastly, we describe how our model achieves dynamic novel view synthesis through a progressive learning framework. An overview of our model is illustrated in Fig. 1.

3.1. Sparse-Controlled Gaussian Extraction

Sparse-Controlled Gaussian extraction module involves augmenting the original *sparse* 3D Gaussians to a set of *dense* 3D Gaussians. For each sparse point $\mathcal{P}_{\text{sparse}}$ computed from SfM, we employ KNN [29] to identify the K nearest control points and generate additional \mathcal{N}_p Gaussian points, sampled randomly within the minimum and maximum value of the position of each existing point clouds. These boundaries determine the extent to which new dense Gaussians can be distributed around each original point. We remove points exceeding a predefined nearest-neighbor distance threshold, t_d , effectively controlling point density and preventing excessive allocations or overestimations. The newly generated points \mathcal{P}_{KNN} are assigned color based on the nearest neighboring sparse 3D Gaussians. The final set of *dense* Gaussians is obtained by combining the generated point clouds with the original sparse points: $\mathcal{P}_{\text{dense}} = \mathcal{P}_{\text{sparse}} + \mathcal{P}_{\text{KNN}}$. Then, using the updated Gaussians, we perform two variety of motion estimations.

3.2. Object Motion Estimation with Deblurring

Object Motion blur arises when objects move through space at velocities exceeding the human eye to capture full visual fidelity. Accordingly, object motion estimation involves modeling actual physical movements to learn the transformations that modify its geometry.

Similar to Lee et al. [16], we produce M additional sets of Gaussians by introducing small positional offsets to each dense Gaussian points $\mathcal{P}_{\text{dense}}$. We then employ an MLP that take center position μ_j , rotation r_j , scale s_j , and camera view p , along with its positional encoding γ , which outputs the transformed scaling factors of the i th predicted Gaussian points as $\{(\delta\mu_{ji}, \delta r_{ji}, \delta s_{ji})\}_{i=1}^M = \mathcal{F}_\theta(\gamma(\mu_j), r_j, s_j, \gamma(p))$.

The scaling factors are refined to obtain the transformed 3D Gaussians $G^*(\hat{\mu}_j, \hat{r}_j, \hat{s}_j)$ that model the blurriness caused by dynamic object motions as follows:

$$\hat{\mu}_{ji} = \mu_j + \lambda_p \delta\mu_{ji}, \quad (1a)$$

$$\hat{r}_{ji} = r_j \cdot \rho_r \cdot \min(1.0, \lambda_q \delta r_{ji} + (1 - \lambda_q)) \quad (1b)$$

$$\hat{s}_{ji} = s_j \cdot \rho_s \cdot \min(1.0, \lambda_q \delta s_{ji} + (1 - \lambda_q)), \quad (1c)$$

where each set represents to 3D Gaussians from different

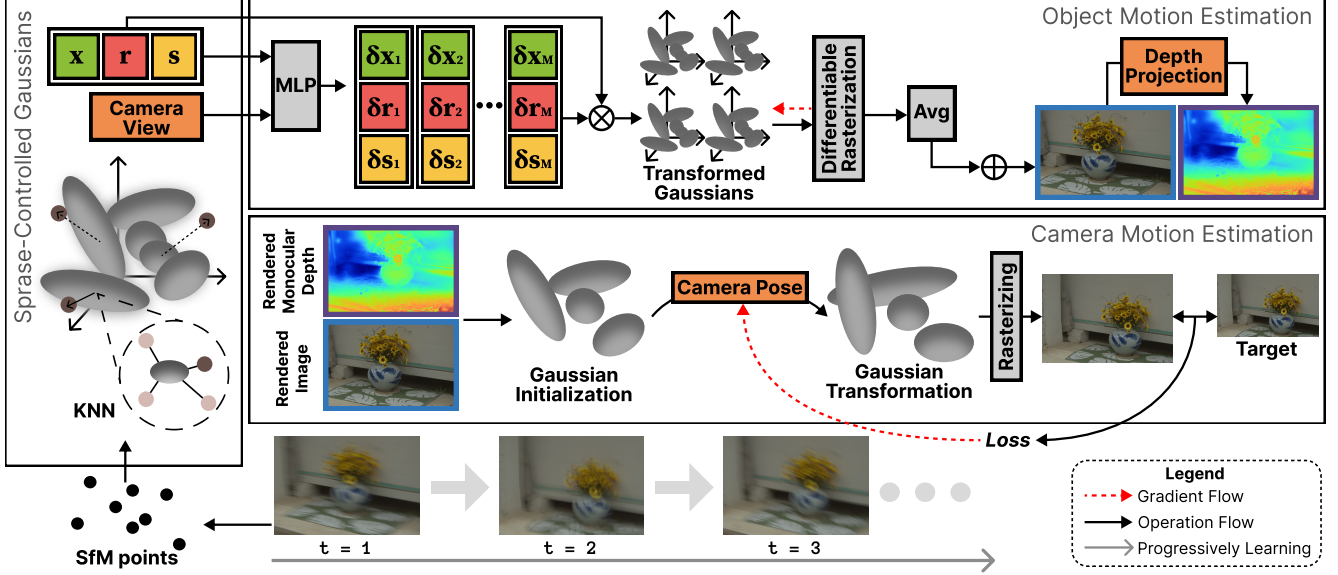


Figure 1. **Overview.** Given a sequence of unposed images and known camera intrinsics, our model recovers camera poses and synthesizes a sharp, photorealistic scene. We take a sequence of blurry images to learn sparse 3D Gaussian points, which are refined into dense Gaussian points via a K-Nearest Neighbor (KNN) search. These sparse-controlled 3D Gaussians are then used to estimate object motion and optimize camera poses via Gaussian transformations and color-consistent rendering. By minimizing photometric loss and positional loss during rendering, the model iteratively refines the 3D Gaussian representations as the camera moves.

viewpoints and is optimized during training to model blurriness caused by dynamic object movements.

The transformed Gaussians $G^*(\hat{\mu}_j, \hat{r}_j, \hat{s}_j)$ model motion-blurred scenes more flexibly as each Gaussian position, rotation, and scale factor are estimated. From a practical perspective, defocus blur often occurs alongside motion blur due to the spatial characteristics of the environment. Therefore, the scaling factors are essential to reduce blurriness and improve motion estimation performance.

We render M clean images from M distinct input views of dense 3D Gaussians G^* , which are then averaged to generate object motion deblurred images I using a differentiable rasterizer \mathcal{R} . During inference, no additional scaling factors are used for image rendering, thus, \mathcal{F}_θ is not activated, enabling real-time rendering of sharp images. In the subsequent step, our method leverages the depth information derived from the rendered scene to estimate the camera motion. The transformed attributes are utilized to compute the depth of the rendered 3D Gaussian scene as:

$$\hat{D} = \sum_{i \in \mathcal{N}} d_i \alpha_i T_i \quad \text{with} \quad T_i = \prod_{j=1}^{i-1} (1 - \alpha_j), \quad (2)$$

where d_i is the depth of the mean of the Gaussian point, which is the z -coordinate of the position projected into the image view space as $d_i = (r_i p_i + T_i)_z$.

3.3. Camera Motion Estimation

We initialize 3DGS using the estimated rendered view and its monocular depth. Following Fu et al. [9], the mean μ of 3D Gaussians is projected onto the 2D image plane as $\mu_{2D} = K(W\mu)/(W\mu)_z$, where K represents the intrinsic projection matrix and W the viewing transformation matrix. Consequently, estimating the camera pose is equivalent to determining the transformation of the 3D rigid Gaussians.

The pretrained Gaussians G_t^* are transformed by a learnable $SE(3)$ transformation into the subsequent frame G_{t+1}^* , as $G_{t+1}^* = \mathbf{T}_t \odot G_t^*$, with an assumption that the camera moves in an arbitrary but smooth trajectory. Mathematically, the optimization can be formulated as:

$$\Theta^*, \Pi^* = \operatorname{argmin}_{\Theta, \Pi} \mathcal{L}_{\text{image}}(\mathcal{R}(G_{t+1}^*), I_{t+1}), \quad (3)$$

which is trained to minimize the photometric loss between the rendered image G_{t+1}^* and the next frame I_{t+1} with the camera parameters Π and 3D Gaussian parameters Θ that are updated during optimization. During optimization, we freeze all attributes of the pretrained 3D Gaussians.

3.4. Model Training

We optimize our approach with the following objective:

$$\mathcal{L} = \mathcal{L}_{\text{image}} + \lambda_{\text{depth}} \mathcal{L}_{\text{depth}} + \lambda_{\text{pose}} \mathcal{L}_{\text{pose}}, \quad (4a)$$

$$\mathcal{L}_{\text{image}} = \lambda \mathcal{L}_1 + (1 - \lambda) \mathcal{L}_{\text{D-SSIM}}, \quad (4b)$$

$$\mathcal{L}_{\text{pose}} = \|\max(s_j, \epsilon_{\text{pose}})\|_2 \quad (4c)$$

Type	Model	Camellia			Bench			Dragon			Sunflowers			Jars1			Jars2		
		PSNR↑	SSIM↑	LPIPS↓															
id	Deblur-GS[5]	26.67	0.72	0.31	<u>26.89</u>	<u>0.74</u>	0.29	27.40	0.57	<u>0.54</u>	26.87	<u>0.77</u>	0.41	24.49	0.63	0.34	<u>23.46</u>	0.69	0.34
id	Deblurring 3DGS[16]	24.92	0.56	0.53	25.15	0.57	0.59	<u>29.05</u>	0.56	0.65	<u>27.45</u>	0.73	<u>0.39</u>	25.59	0.60	<u>0.44</u>	22.72	0.57	0.52
vs	NoPe-NeRF[3]	23.45	0.57	0.66	23.05	0.64	0.66	28.68	0.61	0.69	26.05	0.73	0.59	24.14	0.63	0.64	22.25	0.67	0.63
vs	GS on the Move[31]	23.50	0.65	0.58	24.46	0.73	0.58	29.29	0.71	0.66	25.67	<u>0.77</u>	0.50	24.46	<u>0.69</u>	0.59	22.46	0.72	0.58
vs	COLMAP-Free[9]	19.60	0.69	0.63	21.72	4.46	0.17	25.79	<u>0.83</u>	0.56	22.90	0.73	0.51	24.86	0.78	0.51	22.37	<u>0.71</u>	0.53
id+vs	Ours	<u>25.98</u>	<u>0.70</u>	<u>0.39</u>	26.99	0.75	<u>0.24</u>	29.31	0.84	0.52	28.51	0.82	0.33	<u>24.95</u>	0.78	0.50	24.11	0.74	<u>0.48</u>

Table 2. Quantitative comparison of dynamic view synthesis on ExBluRF’s real dataset.

Type	Model	Church			Barn			Museum			Horse			Ballroom			Francis		
		PSNR↑	SSIM↑	LPIPS↓	PSNR↑	SSIM↑	LPIPS↓	PSNR↑	SSIM↑	LPIPS↓									
id	Deblur-GS[5]	25.19	0.82	0.19	24.29	0.69	0.34	22.80	0.67	0.29	20.43	0.65	0.39	26.12	0.85	0.13	28.06	0.82	0.27
id	Deblurring 3DGS[16]	22.71	0.75	0.19	28.01	0.91	0.09	33.84	0.95	0.02	27.36	0.88	<u>0.07</u>	31.97	0.95	0.02	33.76	<u>0.92</u>	<u>0.08</u>
vs	NoPe-NeRF[3]	25.17	0.73	0.39	26.35	0.69	0.44	26.77	0.76	0.35	27.64	0.84	0.26	25.33	0.72	0.38	23.96	0.61	0.47
vs	GS on the Move[31]	30.62	0.92	<u>0.07</u>	29.27	0.97	0.06	35.71	0.97	0.02	24.48	0.94	0.10	35.53	0.97	0.02	32.41	0.94	0.10
vs	COLMAP-Free[9]	30.38	<u>0.93</u>	<u>0.09</u>	30.43	<u>0.89</u>	<u>0.11</u>	<u>29.50</u>	0.90	0.10	<u>34.10</u>	<u>0.96</u>	0.05	32.64	<u>0.96</u>	<u>0.05</u>	32.81	<u>0.92</u>	0.14
id+vs	Ours	34.04	0.98	0.02	30.43	<u>0.89</u>	0.09	29.80	0.98	<u>0.08</u>	36.52	0.98	0.014	<u>35.01</u>	0.97	0.02	<u>33.20</u>	0.93	0.06

Table 3. Quantitative comparison of dynamic view synthesis on Tanks and Temples’ real dataset. †: Results from paper.

Type	Model	Church			Barn			Museum			Horse			Ballroom			Francis		
		RPE _t ↓	RPE _r ↓	ATE↓	RPE _t ↓	RPE _r ↓	ATE↓	RPE _t ↓	RPE _r ↓	ATE↓	RPE _t ↓	RPE _r ↓	ATE↓	RPE _t ↓	RPE _r ↓	ATE↓	RPE _t ↓	RPE _r ↓	ATE↓
vs	NoPe-NeRF†[3]	0.034	0.008	0.008	0.0046	0.032	0.004	0.207	0.202	0.020	0.179	0.017	0.003	0.041	0.018	0.002	0.057	0.009	0.005
vs	COLMAP-Free[9]	0.012	0.018	0.002	0.040	0.034	0.004	0.052	0.215	0.004	0.112	0.057	0.003	0.037	0.017	0.003	0.029	0.154	0.006
id+vs	Ours	0.011	0.018	0.002	0.039	0.036	0.004	0.051	0.202	0.004	0.101	0.046	0.001	0.030	0.009	0.002	0.025	0.102	0.006

Table 4. Quantitative results of camera pose estimation on Tanks and Temples. We exclude results from GS on the Move, as this model primarily targets smartphone data or basic synthetic datasets and does not record external pose-related sources. †: Results from paper.

where $\lambda_{\text{depth}} = 0.01$ and $\lambda_{\text{pose}} = 1$. The image loss combines L1 and D-SSIM terms, weighted by $\lambda = 0.2$. The pose loss regularizes the position scale of each Gaussian using its scaling factor, with ϵ_{pose} controlling tolerance to minor localization errors in the original Gaussian points. Please refer to the supplementary materials for full details.

4. Experiment

In this section, we evaluate our experiments using the ExBluRF [18] and Tanks and Temples [15] real camera motion datasets, comparing it against five models listed in Tab. 1. For novel view synthesis evaluation, we report the standard metrics: PSNR [11], SSIM [34], and LPIPS [39]. For camera pose estimation, we measure Absolute Trajectory Error (ATE) and Relative Pose Error (RPE), in terms of their rotation (r) and translation (t).

4.1. Results on Dynamic View Synthesis

As illustrated in Tab. 2, our method achieves accurate view synthesis from blurry monocular video on the ExBluRF dataset. In contrast, baselines struggle to handle scene blurriness, often producing inaccurate sharp reconstructions, particularly in densely clustered regions where occluded or ambiguous objects overlap. Furthermore, our method out-

performs existing models in the Tanks and Temples dataset, as demonstrated in Tab. 3. The dataset’s diversity of indoor and outdoor environments highlights the robustness of our approach in synthesizing complex scenes.

4.2. Results on Camera Motion Estimation

Following Fu et al. [9], we refine the estimated camera poses using Procrustes analysis and compared them with the ground-truth poses from the training views. Experimental results demonstrate that jointly handling image deblurring and pose optimization maintains performance and, in fact, surpasses baselines on the Tank and Temples in Tab. 4.

Due to space constraints, qualitative results for dynamic view synthesis and camera motion estimation, including pose trajectory, are provided in the supplementary material.

5. Conclusion

In this paper, we present DBMovi-GS, a method for dynamic view synthesis from blurry monocular video, addressing the limitations of prior approaches in handling dynamic objects. By densifying the initial point clouds and employing Gaussian representations to jointly model object and camera motion, our method achieves highly detailed, consistent, and realistic reconstructions of dynamic scenes.

References

- [1] Benjamin Attal, Selena Ling, Aaron Gokaslan, Christian Richardt, and James Tompkin. Matryodshka: Real-time 6dof video view synthesis using multi-sphere images. In *European Conference on Computer Vision*, pages 441–459. Springer, 2020. 2
- [2] Aayush Bansal, Minh Vo, Yaser Sheikh, Deva Ramanan, and Srinivasa Narasimhan. 4d visualization of dynamic events from unconstrained multi-view videos. In *Proceedings of the IEEE/CVF Conference on Computer Vision and Pattern Recognition*, pages 5366–5375, 2020. 2
- [3] Wenjing Bian, Zirui Wang, Kejie Li, Jia-Wang Bian, and Victor Adrian Prisacariu. Nope-nerf: Optimising neural radiance field with no pose prior. In *Proceedings of the IEEE/CVF Conference on Computer Vision and Pattern Recognition*, pages 4160–4169, 2023. 1, 4, 2, 3
- [4] Minh-Quan Viet Bui, Jongmin Park, Jihyong Oh, and Munchurl Kim. Dyblurf: Dynamic deblurring neural radiance fields for blurry monocular video. *arXiv preprint arXiv:2312.13528*, 2023. 2
- [5] Wenbo Chen and Ligang Liu. Deblur-gs: 3d gaussian splatting from camera motion blurred images. *Proceedings of the ACM on Computer Graphics and Interactive Techniques*, 7(1):1–15, 2024. 1, 2, 4
- [6] Yilun Du, Yanan Zhang, Hong-Xing Yu, Joshua B Tenenbaum, and Jiajun Wu. Neural radiance flow for 4d view synthesis and video processing. In *CVF International Conference on Computer Vision (ICCV)*, pages 14304–14314, 2021. 2
- [7] Yuanxing Duan, Fangyin Wei, Qiyu Dai, Yuhang He, Wenzheng Chen, and Baoquan Chen. 4d gaussian splatting: Towards efficient novel view synthesis for dynamic scenes. *arXiv preprint arXiv:2402.03307*, 2024. 1, 2
- [8] Yalda Foroutan, Daniel Rebain, Kwang Moo Yi, and Andrea Tagliasacchi. Evaluating alternatives to sfm point cloud initialization for gaussian splatting, 2024. 1, 3
- [9] Yang Fu, Sifei Liu, Amey Kulkarni, Jan Kautz, Alexei A. Efros, and Xiaoqiang Wang. Colmap-free 3d gaussian splatting, 2024. 1, 2, 3, 4
- [10] Xavier Glorot and Yoshua Bengio. Understanding the difficulty of training deep feedforward neural networks. In *Proceedings of the Thirteenth International Conference on Artificial Intelligence and Statistics*, pages 249–256, Chia Laguna Resort, Sardinia, Italy, 2010. PMLR. 3
- [11] Quan Huynh-Thu and Mohammed Ghanbari. Scope of validity of psnr in image/video quality assessment. *Electronics letters*, 44(13):800–801, 2008. 4
- [12] Muhammad Zubair Irshad, Sergey Zakharov, Katherine Liu, Vitor Guizilini, Thomas Kollar, Adrien Gaidon, Zsolt Kira, and Rares Ambrus. Neo 360: Neural fields for sparse view synthesis of outdoor scenes, 2023. 2
- [13] Ramesh Jain, Rangachar Kasturi, and Brian G. Schunck. *Machine vision*. McGraw-Hill, Inc., USA, 1995. 2
- [14] Bernhard Kerbl, Georgios Kopanas, Thomas Leimkühler, and George Drettakis. 3d gaussian splatting for real-time radiance field rendering, 2023. 1, 2
- [15] Arno Knapitsch, Jaesik Park, Qian-Yi Zhou, and Vladlen Koltun. Tanks and temples: benchmarking large-scale scene reconstruction. *ACM Trans. Graph.*, 36(4), 2017. 4, 1
- [16] Byeonghyeon Lee, Howoong Lee, Xiangyu Sun, Usman Ali, and Eunbyung Park. Deblurring 3d gaussian splatting. *arXiv preprint arXiv:2401.00834*, 2024. 1, 2, 4
- [17] Dogyoon Lee, Minhyeok Lee, Chajin Shin, and Sangyoun Lee. Dp-nerf: Deblurred neural radiance field with physical scene priors. In *Proceedings of the IEEE/CVF Conference on Computer Vision and Pattern Recognition*, pages 12386–12396, 2023. 2
- [18] Dongwoo Lee, Jeongtaek Oh, Jaesung Rim, Sunghyun Cho, and Kyoung Mu Lee. Exblurf: Efficient radiance fields for extreme motion blurred images. In *Proceedings of the IEEE/CVF International Conference on Computer Vision*, pages 17639–17648, 2023. 2, 4, 1
- [19] Tianye Li, Mira Slavcheva, Michael Zollhoefer, Simon Green, Christoph Lassner, Changil Kim, Tanner Schmidt, Steven Lovegrove, Michael Goesele, Richard Newcombe, et al. Neural 3d video synthesis from multi-view video. In *Proceedings of the IEEE/CVF Conference on Computer Vision and Pattern Recognition*, pages 5521–5531, 2022. 2
- [20] Zhengqi Li, Simon Niklaus, Noah Snavely, and Oliver Wang. Neural scene flow fields for space-time view synthesis of dynamic scenes. In *Proceedings of the IEEE/CVF Conference on Computer Vision and Pattern Recognition*, pages 6498–6508, 2021. 2
- [21] Zhan Li, Zhang Chen, Zhong Li, and Yi Xu. Spacetime gaussian feature splatting for real-time dynamic view synthesis. In *Proceedings of the IEEE/CVF Conference on Computer Vision and Pattern Recognition*, pages 8508–8520, 2024. 1, 2
- [22] Zhicheng Lu, Xiang Guo, Le Hui, Tianrui Chen, Min Yang, Xiao Tang, Feng Zhu, and Yuchao Dai. 3d geometry-aware deformable gaussian splatting for dynamic view synthesis. In *Proceedings of the IEEE/CVF Conference on Computer Vision and Pattern Recognition*, pages 8900–8910, 2024. 1
- [23] Jonathon Luiten, Georgios Kopanas, Bastian Leibe, and Deva Ramanan. Dynamic 3d gaussians: Tracking by persistent dynamic view synthesis. *arXiv preprint arXiv:2308.09713*, 2023. 2
- [24] Achleshwar Luthra, Shiva Souhith Gantha, Xiyun Song, Heather Yu, Zongfang Lin, and Liang Peng. Deblur-nsff: Neural scene flow fields for blurry dynamic scenes. In *Proceedings of the IEEE/CVF Winter Conference on Applications of Computer Vision*, pages 3658–3667, 2024. 2
- [25] Li Ma, Xiaoyu Li, Jing Liao, Qi Zhang, Xuan Wang, Jue Wang, and Pedro V Sander. Deblur-nerf: Neural radiance fields from blurry images. In *Proceedings of the IEEE/CVF Conference on Computer Vision and Pattern Recognition*, pages 12861–12870, 2022. 2
- [26] Ben Mildenhall, Pratul P Srinivasan, Matthew Tancik, Jonathan T Barron, Ravi Ramamoorthi, and Ren Ng. Nerf: Representing scenes as neural radiance fields for view synthesis. *Communications of the ACM*, 65(1):99–106, 2021. 2
- [27] Norman Müller, Katja Schwarz, Barbara Rössle, Lorenzo Porzi, Samuel Rota Bulò, Matthias Nießner, and Peter

- Kontschieder. Multidiff: Consistent novel view synthesis from a single image. In *Proceedings of the IEEE/CVF Conference on Computer Vision and Pattern Recognition*, pages 10258–10268, 2024. 1
- [28] Byeongjun Park and Changick Kim. Point-dynrf: Point-based dynamic radiance fields from a monocular video. In *Proceedings of the IEEE/CVF Winter Conference on Applications of Computer Vision*, pages 3171–3181, 2024. 2
- [29] Leif Peterson. K-nearest neighbor. *Scholarpedia*, 4:1883, 2009. 2
- [30] Johannes L Schonberger and Jan-Michael Frahm. Structure-from-motion revisited. In *Proceedings of the IEEE conference on computer vision and pattern recognition*, pages 4104–4113, 2016. 1
- [31] Otto Seiskari, Jerry Ylilammi, Valtteri Kaatrasalo, Pekka Rantalankila, Matias Turkulainen, Juho Kannala, and Arno Solin. Gaussian splatting on the move: Blur and rolling shutter compensation for natural camera motion, 2024. 1, 4, 2
- [32] Noah Snavely, Steven M. Seitz, and Richard Szeliski. Photo tourism: exploring photo collections in 3d. *ACM Trans. Graph.*, 25(3):835–846, 2006. 1
- [33] Peng Wang, Lingzhe Zhao, Ruijie Ma, and Peidong Liu. Bad-nerf: Bundle adjusted deblur neural radiance fields. In *Proceedings of the IEEE/CVF Conference on Computer Vision and Pattern Recognition*, pages 4170–4179, 2023. 1, 2
- [34] Zhou Wang, Alan C Bovik, Hamid R Sheikh, and Eero P Simoncelli. Image quality assessment: from error visibility to structural similarity. *IEEE transactions on image processing*, 13(4):600–612, 2004. 4
- [35] Daniel Watson, William Chan, Ricardo Martin-Brualla, Jonathan Ho, Andrea Tagliasacchi, and Mohammad Norouzi. Novel view synthesis with diffusion models. *arXiv preprint arXiv:2210.04628*, 2022. 1
- [36] Jianfeng Xiang, Jiaolong Yang, Binbin Huang, and Xin Tong. 3d-aware image generation using 2d diffusion models. In *Proceedings of the IEEE/CVF International Conference on Computer Vision*, pages 2383–2393, 2023. 1
- [37] Yawen Xiang, Heng Zhou, Chengyang Li, Fangwei Sun, Zhongbo Li, and Yongqiang Xie. Application of deep learning in blind motion deblurring: Current status and future prospects. *arXiv preprint arXiv:2401.05055*, 2024. 3
- [38] Zeyu Yang, Hongye Yang, Zijie Pan, Xiatian Zhu, and Li Zhang. Real-time photorealistic dynamic scene representation and rendering with 4d gaussian splatting. *arXiv preprint arXiv:2310.10642*, 2023. 2
- [39] Richard Zhang, Phillip Isola, Alexei A Efros, Eli Shechtman, and Oliver Wang. The unreasonable effectiveness of deep features as a perceptual metric. In *Proceedings of the IEEE conference on computer vision and pattern recognition*, pages 586–595, 2018. 4
- [40] Kaichen Zhou, Jia-Xing Zhong, Sangyun Shin, Kai Lu, Yiyuan Yang, Andrew Markham, and Niki Trigoni. Dynpoint: Dynamic neural point for view synthesis. *Advances in Neural Information Processing Systems*, 36, 2024. 2

DBMovi-GS: Dynamic View Synthesis from Blurry Monocular Video via Sparse-Controlled Gaussian Splatting

Supplementary Material

Within the supplementary material, we provide:

- Pseudocode of our proposed Sparse-Controlled Gaussian Extraction framework in Sec. 6.
- Implementation details, including hyperparameters and training details in Sec. 7.
- Further description of the datasets and baselines, including training specifics, in Secs. 8 and 9, respectively.
- Detailed procedure of our proposed method in Sec. 10
- Qualitative results for dynamic view synthesis and camera pose estimation in Sec. 11.
- Ablation studies on the loss function and the Gaussian splats in Sec. 12

6. Sparse-Controlled Gaussian Pseudocode

Algorithm 1 Sparse-Controlled Gaussian Initialization

Require: Sparse points $\mathcal{P}_{\text{sparse}}$
Require: Number of new points N_p
Require: KNN parameter K
Require: Distance threshold t_d
Ensure: Dense points $\mathcal{P}_{\text{dense}}$

- 1: **for** each point $p \in \mathcal{P}_{\text{sparse}}$ **do**
- 2: Uniformly sample \mathcal{N}_p new points to form \mathcal{P}_{new} .
- 3: **for** each point $p_{\text{new}} \in \mathcal{P}_{\text{new}}$ **do**
- 4: Identify K nearest neighbors \mathcal{N}_K from $\mathcal{P}_{\text{sparse}}$
- 5: Compute distances $d(p_{\text{new}}, \mathcal{N}_K)$
- 6: **if** $\min d(p_{\text{new}}, \mathcal{N}_K) > t_d$ **then**
- 7: Discard p_{new}
- 8: **else**
- 9: Assign interpolated properties to p_{new}
- 10: Add p_{new} to \mathcal{P}_{KNN}
- 11: **end if**
- 12: **end for**
- 13: **end for**
- 14: $\mathcal{P}_{\text{dense}} = \mathcal{P}_{\text{sparse}} + \mathcal{P}_{\text{KNN}}$
- 15: **return** $\mathcal{P}_{\text{dense}}$

7. Implementation Details

7.1. Motion Estimation

The positional encoding utilized for the scaling factors during object motion estimation incorporates two key features: multi-frequency representation and dimensionality expansion. We adopt a sinusoidal positional encoding following the approach in Lee et al. [16], employing frequencies

of $2^k\pi$ and dimensionality of $2L$ for each encoding. This design enables the model to effectively capture coarse and fine-grained positional information, which is essential for accurately modeling object motion at varying scales and complexities.

Given the high proximity between consecutive frames, the associated transformations are relatively small, allowing for efficient optimization. Additionally, the pose estimation step leverages this efficient encoding to achieve precise results within a runtime of less than a minute. This streamlined process not only minimizes the computational overhead but also ensures scalabilities for processing large datasets with complex and dynamic motion patterns.

8. Dataset Details

8.1. ExBluRF

ExBluRF [18] presents challenging motion-blurred images by incorporating random 6-DOF camera motion trajectories. Each scene in this dataset comprises 29 blurry training images and 5 sharp test images. The real datasets from ExBluRF were acquired using a dual-camera system; one camera captured a single blurry image with a long exposure time, while the other recorded a sequence of sharp images during the same exposure. A total of eight scenes were captured, with each scene containing between 20 to 40 multi-view blurry images along with their corresponding sequences of sharp images.

8.2. Tanks and Temples

The Tanks and Temples [15] dataset assesses the quality of view synthesis and the accuracy of pose estimation, which include both indoor and outdoor environments. We use the real dataset version only and sample 7 images from every 8-frame clip for training per scene, reserving the remaining images to test the quality of view synthesis. Camera poses are estimated and evaluated using all training samples. Tab. 5 provides details about the video sequences for each scene in the Tanks and Temples benchmark.

9. Baseline Details

We outline the preprocessing and setup procedures applied to the baseline models, including the additional adaptations required to align them with our experimental conditions. Technical specifications are also detailed.

Scene	Type	Frame rate (fps)	Max. rotation (deg)
Church	indoor	30	37.3°
Barn	outdoor	20	47.5°
Museum	indoor	20	76.2°
Horse	outdoor	30	39.0°
Ballroom	indoor	20	30.3°
Francis	outdoor	20	47.5°

Table 5. Details of training sequences of Tanks and Temples dataset. Fps denotes frame per second per scene. Max. rotation denotes the maximum relative rotation angle, in degrees, between two frames in the selected sequence.

9.1. Deblur-GS

Deblur-GS [5] only supports `SIMPLE_PINHOLE` and does not support the `SIMPLE_RADIAL` model used in the Tanks dataset. Both refer to specific camera models used during 3D reconstruction, typically implemented in COLMAP or similar structure-from-motion tools. When extracting camera poses from COLMAP, images are not transformed according to the strict distortion model; instead, the field of view (FOV) is utilized directly. Following the configuration of NoPe-NeRF, we applied the same approach in Deblur-GS, calculating the field of view in the same manner as the specific camera model used during 3D reconstruction.

9.2. Gaussian Splatting on the Move

As outlined in the original paper [31], for the datasets lacking camera poses or 3D point cloud data (*i.e.*, `transform.json` in the Nerfstudio format), we process raw benchmark input data using the provided Python script. Specifically, COLMAP was employed to reconstruct point clouds and generate camera poses from blurry image sequences (*i.e.*, `sparse.pc` and `transform.json`). One explanation for the findings in the new study is that extracting feature points from blurry images often required multiple attempts to ensure successful reconstruction. The training was conducted exclusively on blurry image samples, with sharp images reserved for evaluation to assess the prediction of sharp outputs. Training for a single image sequence typically converged within 12000 epochs, with total training time generally under one hour per sequence, depending on the dataset. At present, no code is provided for computing pose estimation errors, as the focus of the study is on smartphone data, with no intention to analyze the intricacies of pose estimation in this context. The experimental setup was implemented on Ubuntu 20.04 using a Conda environment with Python 3.8.20, CUDA 12.1, and six RTX 3090 GPUs, each equipped with 24GB of VRAM.

9.3. NoPe-NeRF

For the NoPe-NeRF [3] dataset, the experimental setup utilized Ubuntu 20.04, a Conda environment with Python 3.9.18, CUDA 12.1, and six RTX 3090 GPUs, each featuring 24GB of VRAM. During preprocessing, depth maps were generated for each image within the provided image sequences. The model included camera pose and point cloud reconstruction data, eliminating the need for external reconstruction methods. Training times varied by dataset but generally required less than 1.5 days per scene. The evaluation was conducted using sharp images to assess the predicted sharp outputs. Early stopping was applied during training, with convergence typically achieved in fewer than 10000 epochs for each sequence.

10. Method Details

10.1. Preliminaries

3D Gaussian Splatting. 3DGS [14] represents a volumetric scene as a set of 3D Gaussians. A scene is parameterized as a set of Gaussian points with center position μ , opacity σ , and sphere harmonics coefficient sh . Each 3D Gaussian is defined by a 3D covariance matrix and its center position μ , which is referred to as the mean value of the Gaussian:

$$G(x, r, s) = \exp\left(-\frac{1}{2}x^T\Sigma^{-1}(r, s)x\right). \quad (5)$$

For differentiable optimization, the covariance matrix is decomposed into two learnable components as $\Sigma(r, s) = RSS^T R^T$, where R is for rotation quaternion and S is for scaling parameter. These 3D Gaussians are projected into 2D image space to obtain a 2D covariance matrix in camera coordinates $\Sigma(r, s)'$ for rendering via viewing transformation matrix W and Jacobian of the affine approximation of the projective transformation J :

$$\Sigma(r, s)' = JW\Sigma(r, s)W^T J^T. \quad (6)$$

After projection, each pixel is computed by blending the N ordered points that overlap the 2D Gaussian pixel as:

$$\hat{C} = \sum_{i=1}^N c_i \alpha_i T_i, \quad \text{where} \quad T_i = \prod_{j=1}^{i-1} (1 - \alpha_j). \quad (7)$$

where c_i and α_i represent the color and density of each point computed by a 3D Gaussian with covariance matrix multiplied by per-point opacity and sh color coefficients.

Image Deblurring. Image blur is a common manifestation of camera shake or defocus, which occurs when the shutter speed is insufficient to maintain a stable camera pose or the light ray from a scene point forms a circle of confusion on the camera lens [13]. Image deblurring involves removing the blurring artifacts from images to restore the

original content. Among diverse applications of deep learning in deblurring, we address three types of blur frequently encountered in real-world scenarios [37].

Object motion blur arises from the relative motion between an object and the camera system during exposure, which occurs when capturing fast-moving objects or with long exposure times. *Camera motion blur* is caused by the camera’s motion during exposure, common in photography or low-light conditions, such as indoors or at night. This blur effect can be complex due to unpredictable hand movements, leading to in-plane or out-of-plane camera translations. *Defocus blur* occurs when parts of a scene fall outside the camera’s depth of field, the range where objects appear sharp. Defocus blur is relatively easy to handle as it involves adjusting the geometry of each 3D Gaussian. In contrast, camera and object motion blur arise from natural or intentional physical movements.

10.2. Sparse Gaussian Extraction

For blurry input images, 3DGS often produces large Gaussians or fails to capture distant points along the object edges, leading to a loss of essential details required for sharp image generation. This ambiguity in Gaussian points, stemming from their dependence on high-quality point cloud initialization from COLMAP, poses challenges in practical applications with large-scale, complex dynamic motions [8]. Thus, it hinders a new approach for point initialization and extraction that captures useful information from blurry monocular images, thereby reducing reliance on COLMAP for photorealistic dynamic view synthesis.

10.3. Object Motion Estimation

The object motion estimation is formulated as follows:

$$I_{\text{pred}}^i = \mathcal{R}(\{G^*(\hat{\mu}_{ji}, \hat{r}_{ji}, \hat{s}_{ji})\}_{j \in \mathcal{P}_{\text{dense}}}), \quad (8)$$

where the scaling factors are adjusted by parameter λ , clipped, and element-wise multiplied with the original Gaussian factors to obtain its transformed sets. Unlike previous methods that model object motion blur and defocus blur separately, our approach introduces an additional set of Gaussians with two learnable parameters, ρ_r for rotation and ρ_s for scale, enabling Gaussian covariance modeling based on scaling factors. These parameters play a pivotal role in simultaneously reducing noise from complex object motion and effectively addressing defocus deblurring.

10.4. Camera Motion Estimation

Camera motion blur, often resulting from camera shake, occurs when the shutter speed is insufficient to maintain a stable pose. Recent approaches demonstrate that estimating camera poses and rendering images can be achieved simultaneously, making pose estimation effectively equivalent to determining 3D rigid transformations [3, 9]. Leveraging

this insight, our model explicitly approximates the camera motion trajectory and optimizes a global transformation for all Gaussians for each camera, without relying on SfM.

In general, the camera parameters include camera intrinsics, poses, and lens distortions. In our work, we utilize camera poses only, such that camera pose for frame I_i is a transformation $\mathbf{T}_i = [\mathbf{q}_i | \mathbf{t}_i]$ that comprises a rotation $\mathbf{q}_i \in \text{SO}(3)$ and a translation $\mathbf{t}_i \in \mathbb{R}^3$.

10.5. Model Training

Progressively Learning. Applying the aforementioned technique to each pair of images determines the relative pose between the initial frame and any subsequent frame at timestep t . However, noise in the relative poses can hinder the optimization of the Gaussian models for the entire scene. To address this issue, we follow Fu et al. [9] by estimating the relative pose between I_{t+1} and I_{t+2} when the next frame I_{t+2} becomes available. The global Gaussian points are updated over the whole iteration utilizing the estimated relative pose and the two observed frames. The progressive learning approach continuously refines the scene by leveraging the sequential nature of video frames. The global points expand the 3D Gaussian representation, better capturing complex camera movements and enabling accurate pose estimation during novel view synthesis.

A fundamental hypothesis underlying our approach is that the scales should be consistent. While points are initialized at their centers and new points are added in proximity to the existing ones, these primitives may diverge from their parent points after the optimization. Although $\mathcal{L}_{\text{image}}$ alone yields comparable rendering results without the need for additional supervision, we leverage depth loss $\mathcal{L}_{\text{depth}}$ to minimize the prediction error associated with the depth estimation from the depth projector (*ref.* Eq. (2)).

We employ the Adam optimizer with a learning rate of 1×10^3 for the MLP and 1.6×10^4 for 3D Gaussians. For the real camera motion blur dataset, the pruning and den-sification thresholds for 3D Gaussians are set to 1×10^{-2} and 5×10^{-4} , respectively. The MLP consists of 4 layers, with the first three layers shared across tasks. These layers extract features that are subsequently fed into three separate output heads, which predict $\delta\mu$, δr , and δs scaling factors. Each layer comprises 64 hidden units, utilizing ReLU activations, and is initialized via Xavier initialization [10]. The regularization parameters, λ_p and λ_s , are both set to 1×10^{-2} . To address point cloud sparsity, additional points are introduced starting from the 2000th iteration. The number of nearest neighbors is set to 4, with a minimum distance threshold set to 2. Depth-based pruning is performed using a multiplier of 3. For camera motion deblurring, the hyper-parameter M is set to 4. Overall, the model is trained for an average of 20000 iterations.

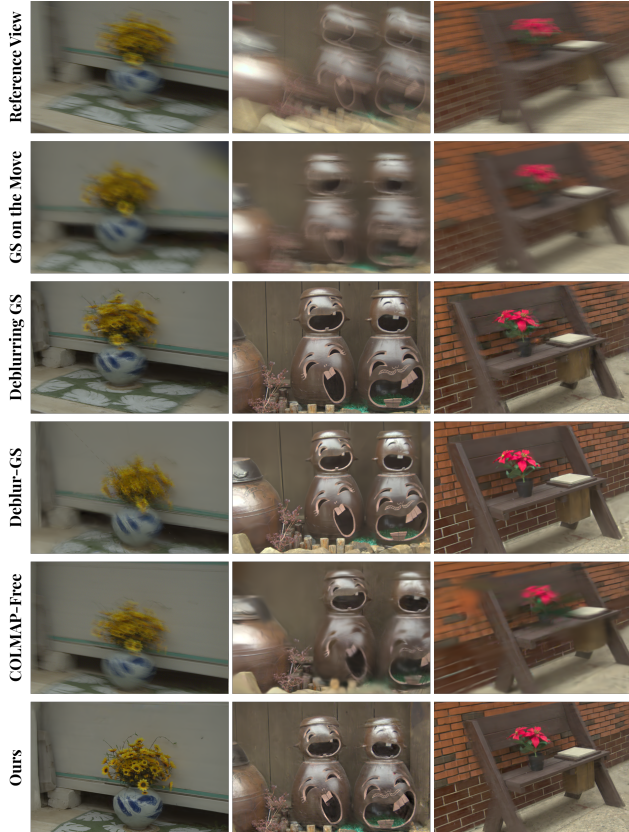


Figure 2. Qualitative comparison of dynamic view synthesis on ExBluRF dataset. We compare our approach against Gaussian-based methods, including GS on the Move[31], Deblurring 3DGS[16], Deblur-GS[5], and COLMAP-Free[9]. Our proposed method effectively reconstructs sharp scenes from blurry inputs, producing fewer artifacts and capturing finer details. Zoom in for a clearer view of the comparison.

11. Qualitative Results

We provide quantitative results on dynamic view synthesis and camera motion estimation in Figs. 2 and 3, respectively.

12. Ablation Studies

We conduct two ablation studies to verify the effectiveness and efficiency of our proposed components.

12.1. Loss Functions

To evaluate the contribution of each loss component, we conduct an ablation by systematically isolating each loss term and assessing its impact. Results in Tab. 6 show that $\mathcal{L}_{\text{image}}$ alone is insufficient for dynamic view synthesis from blurry inputs, with pose loss having a slightly greater impact on performance than depth loss. Depth loss is critical in NeRF-based methods [3], though they hold less importance in Gaussian-based methods.

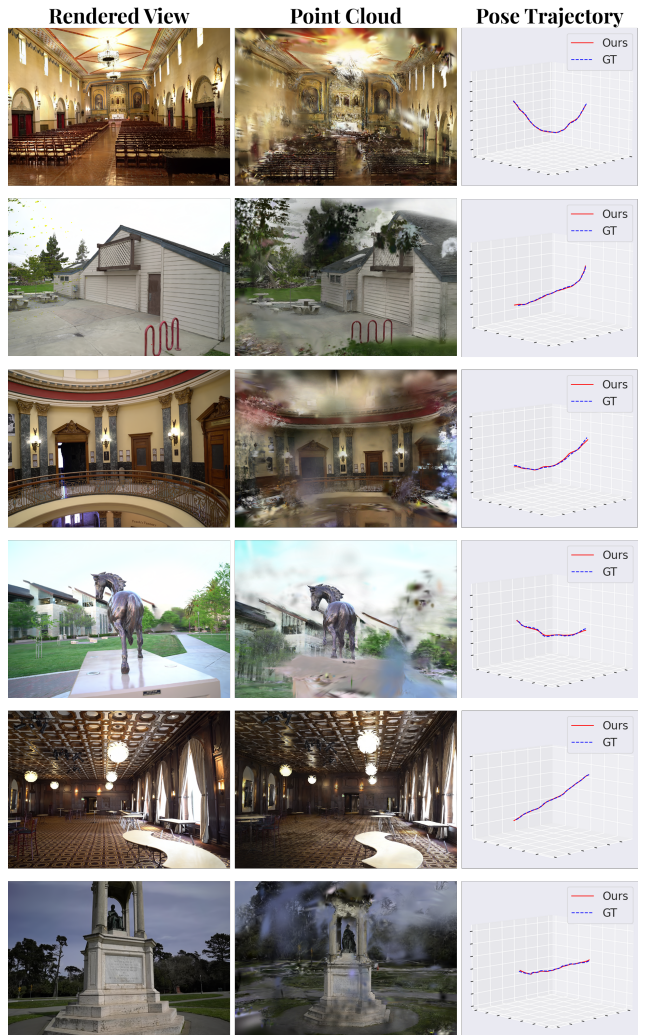


Figure 3. Camera motion estimation results on the Tanks and Temples dataset. For each scene, we present the rendering result (left column), 3D structure from point clouds (middle column), and camera pose estimations (right column). Notably, the ExBluRF dataset is specifically tailored for deblurring tasks that involve dynamic scene reconstruction with significant object motion. However, due to its minimal inherent camera motion, camera pose trajectory assessment is excluded from the evaluation.

12.2. Additional Gaussian Points vs. Training Time

Fig. 4 illustrates the effect of adding dense Gaussians to the sparse Gaussians on the training time. “Before” refers to the sparse Gaussian points initialized from the original 3DGS, while “After” represents the dense Gaussians generated through our module. Our approach is relatively similar to COLMAP-Free [9], exhibiting only a marginal difference in training time while generating dense Gaussian points.

Model	Church (Indoor)			Horse (Outdoor)		
	PSNR \uparrow	SSIM \uparrow	LPIPS \downarrow	PSNR \uparrow	SSIM \uparrow	LPIPS \downarrow
Ours	34.04	0.98	0.02	36.52	0.98	0.01
$\mathcal{L}_{\text{image}}$ only	31.10	0.93	0.09	28.57	0.97	0.05
w/o $\mathcal{L}_{\text{pose}}$	32.99	0.94	0.08	29.40	0.96	0.04

Table 6. Ablation study of each loss component on an indoor and outdoor scene from Tanks and Temples. ‘‘Ours’’ comprises all the loss terms, and ‘‘w/o $\mathcal{L}_{\text{pose}}$ ’’ utilizes photometric and depth losses.

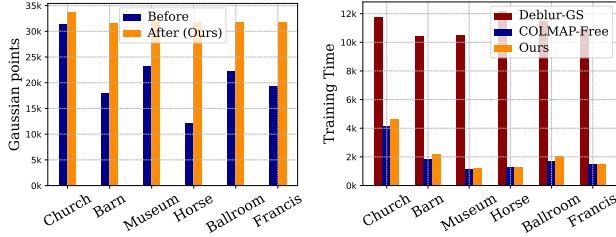


Figure 4. Ablation on the number of Gaussian points after converting from sparse to dense Gaussian points and its impact on training time on Tanks and Temples dataset. Training time is converted from *hrs:min:sec* into a decimal format.

13. Future Work

In future work, we aim to enhance our approach to novel view synthesis by improving its adaptability and practical applicability, specifically extending 3DGS to dynamic scenes through advanced pose optimization. These improvements are expected to further enhance rendering quality and robustness, which includes optimizing computational efficiency to enable real-time performance, particularly in smartphone cameras, facilitating seamless and dynamic scene reconstruction in everyday scenarios.